Engineering Structures 30 (2008) 3412–3425

Contents lists available at ScienceDirect

Engineering Structures

journal homepage: www.elsevier.com/locate/engstruct

Near surface mounted CFRP strips for the flexural strengthening of RC columns: Experimental and numerical research

Joaquim A.O. Barros [a,*], Rajendra K. Varma [a], José M. Sena-Cruz [a], Alvaro F.M. Azevedo [b]

[a] Department of Civil Engineering, University of Minho, Azurém, 4800-058 Guimarães, Portugal

[b] Department of Civil Engineering, University of Porto, Rua Dr. Roberto Frias, 4200-465 Porto, Portugal

ARTICLE INFO

Article history:
Received 21 March 2007
Received in revised form
24 January 2008
Accepted 19 May 2008
Available online 27 June 2008

Keywords:
Near surface mounted reinforcement
Reinforced concrete columns
Strengthening
Carbon fiber reinforced polymer strips
Bending failure
Epoxy adhesive

ABSTRACT

In this work, a strengthening technique based on near surface mounted (NSM) carbon fibre laminate strips bonded into slits opened on the concrete cover is used to improve the flexural capacity of columns subjected to bending and compression. This technique avoids the occurrence of the peeling phenomenon, is able to mobilize the full strengthening capacity of the strips, and provides higher protection against fire and acts of vandalism. We describe the adopted strengthening technique and report the experimental characterization of the materials involved in the strengthening process. The results obtained in two series of reinforced concrete columns, subjected to axial compression and lateral cyclic loading, show that a significant increase on the load carrying capacity can be achieved by using the NSM technique. Cyclic material constitutive laws were implemented in a finite element program and the tests with reinforced concrete columns strengthened with the NSM technique were numerically simulated under cyclic loading. These numerical simulations reproduce the experimental load–displacement diagrams satisfactorily.

© 2008 Elsevier Ltd. All rights reserved.

1. Introduction

Until the last quarter of the twentieth century seismic loading was not generally taken into account in the design of reinforced concrete buildings or, when considered, the resulting reinforcement detailing might not be satisfactory by the standards of the current structural codes. For this reason, significant damage can occur in old buildings, even with the occurrence of moderate seismic loads. In most cases, columns represent the most vulnerable elements since their failure leads to the collapse of the structure.

Since the beginning of the nineties conventional materials used to strengthen reinforced concrete (RC) columns are being replaced with carbon and glass fibre reinforced polymers (CFRP or GFRP). The advantages of these composite materials are the strength/weight and stiffness/weight high ratios, as well as the high resistance to environmental actions, lightness, durability and ease of application [1–4].

In this work a strengthening technique, based on the installation of strips of carbon fibre reinforced polymer (CFRP) laminates into slits opened on the concrete cover of the elements to strengthen, is used to increase the flexural resistance of RC columns failing in bending. These strips have a cross section of 9.6×1.5 mm^2 and are bonded to concrete by means of an epoxy adhesive. This technique is termed near surface mounted (NSM) and its effectiveness in the flexural and shear strengthening of RC beams has been already assessed [5–10].

In recent years a significant amount of research has been undertaken with the aim of accurately modelling the cyclic behaviour of RC columns. An extensive review of available constitutive models and appropriate FEM-based numerical strategies is published elsewhere [11]. The most common approaches regarding the modelling of RC columns with finite elements involve a discretization with 3D solid elements or with Timoshenko beam elements. When 3D solid elements are used, some elements represent concrete and others simulate the reinforcement. For the case of Timoshenko beam elements each cross section is discretized into fibers, corresponding some to the concrete and the remaining to the reinforcement [12]. Models based on 3D solid elements are more suitable to reproduce the behaviour of RC columns subjected to any type of loading such as significant shear forces or torsion. Timoshenko beam based models are less demanding in terms of computational resources but are more appropriate to the simulation of columns mainly subjected to axial and flexural forces.

In the present work, the effectiveness of the NSM technique in the flexural strengthening of RC columns was appraised by means of two series of tests, with different steel reinforcement ratios, subjected to cyclic loading and constant axial compressive

* Corresponding author. Tel.: +351 253510210; fax: +351 253510217.
E-mail addresses: barros@civil.uminho.pt (J.A.O. Barros), rajendra@civil.uminho.pt (R.K. Varma), jsena@civil.uminho.pt (J.M. Sena-Cruz), alvaro@fe.up.pt (A.F.M. Azevedo).

0141-0296/$ – see front matter © 2008 Elsevier Ltd. All rights reserved.
doi:10.1016/j.engstruct.2008.05.019

Notations

The following symbols were used in the paper. Subscript s and c denote steel and concrete respectively.

C/T	Compression /Tension
$E_{c/s}$	Initial Young modulus of concrete/steel
E_{cnew}	Tangent modulus at the new stress point
$E_{so}^{+/-}$	Initial Young's modulus at reversal C/T branch
E_{cpl}	Tangent modulus when the stress is released
$E_{\text{cre}}^{-/+}$	Tangent modulus at the returning point ($\varepsilon_{\text{cre}}^{-/+}$,$f_{\text{cre}}^{-/+}$)
E_{sc}	Tangent modulus of steel
$E_{sh}^{-/+}$	Tangent modulus at strain hardening ($\varepsilon_{sh}^{-/+}$)
E_{st}	Tangent modulus of steel
$E_{t}^{-/+}$	Tangent modulus for concrete on C/T envelope
$f_{c/s}$	Concrete/steel stress
f_{ct}	Peak concrete tension strength
f_{c}'	Peak confined concrete strength
$f_{c}^{-/+}$	Concrete stress on the C/T envelope
$f_{\text{cnew}}^{-/+}$	New stress at the unloading strain for C/T
$f_{\text{cre}}^{-/+}$	Stress at the returning strain ($\varepsilon_{\text{cre}}^{-/+}$)
$f_{\text{csu}}^{-/+}$	Ultimate (maximum) stress during C/T in steel
$f_{\text{cun}}^{-/+}$	Unloading stress from C/T concrete envelope curve
$f_{sy}^{-/+}$	Yield stress during C/T in steel
$n_{c}^{-/+}$	n value for the C/T envelope curve
$R_{so}^{+/-}$	Menegotto–Pinto Eq. parameter
x_{csp}	Non-dimensional spalling strain
$x_{c}^{-/+}$	Non-dimensional strain on the C/T envelope
$x_{cr}^{-/+}$	Non-dimensional critical strain on C/T envelope curve.
ε_{c}	Concrete strain
ε_{c}'	Concrete strain at peak confined stress
$\varepsilon_{so}^{-/+}$	Point of origin of the C/T envelope curve
ε_{cpl}	Plastic strain
$\varepsilon_{\text{cre}}^{-/+}$	Strain at the returning point to the C/T envelope curve
$\varepsilon_{sh}^{-/+}$	Hardening strain during C/T in steel
$\varepsilon_{su}^{-/+}$	Strain at ultimate stress ($f_{su}^{-/+}$)
ε_{t}	Strain at peak tension stress
$\varepsilon_{\text{cun}}^{-/+}$	Unloading strain from C/T concrete envelope curve

load. These tests were numerically simulated with the materially nonlinear algorithms of the FEMIX computer code [13]. In the context of this work, additional cyclic constitutive material models were developed and implemented in the code. The RC columns are discretized with 3D Timoshenko beam elements and each cross section is treated as a set of quadrilateral sub domains (fibrous model, [12]).

In the following sections the experimental and numerical research are described and the main results are presented and discussed.

2. Experimental program

The experimental program carried out in the context of the current work is composed of eight specimens and twelve tests as shown in Table 1. Two series of columns reinforced with longitudinal steel bars of 10 and 12 mm diameter, ϕ_l, were used. The following denominations are adopted: NON series for non-strengthened columns; PRE series for concrete columns strengthened with CFRP strips; POS series for columns of the NON series which were strengthened and then retested. The generic denomination of a series is *Cnm_s*, where *n* represents the diameter of the longitudinal bars, in mm, (10 or 12), *m* is equal to *a* or *b* (*a* and *b* are two tests in similar conditions for statistical purposes), and *s* is equal to NON, PRE or POS.

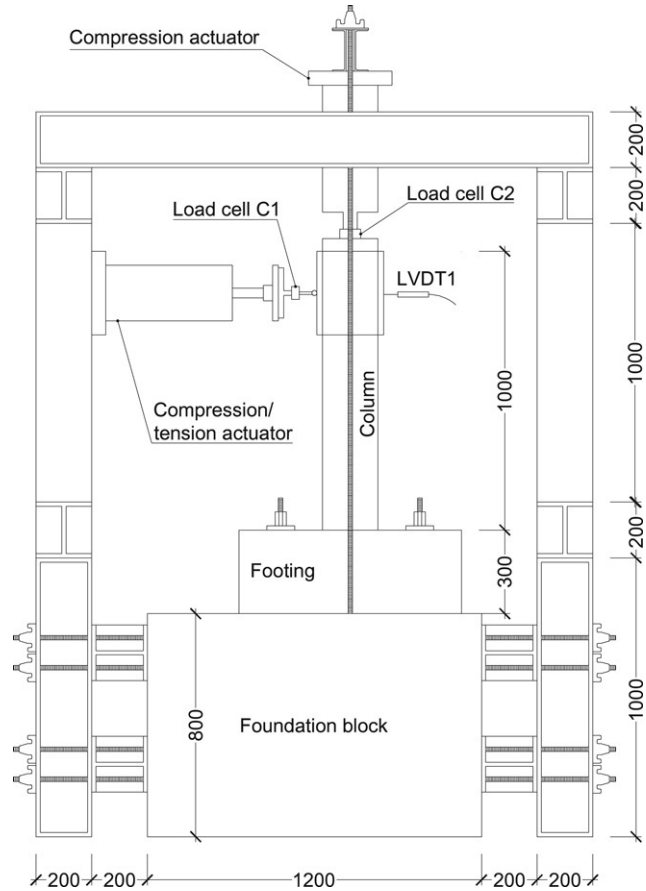

Fig. 1. Test set-up (dimensions in mm).

3. Test setup and testing procedures

The test setup is shown in Fig. 1. Each specimen is composed of a column monolithically connected to a footing, which is fixed to a foundation block by four steel bars. The cyclic horizontal load was applied by means of an actuator having a load capacity of 100 kN. The force was measured using a tension/compression load cell that can reach a maximum load of 250 kN with 0.05% accuracy. This load cell was attached to the piston of the actuator (cell C1 in Fig. 1). To avoid eccentric forces on the actuator, a 3D hinge was placed between the column and the load cell that measures the horizontal force. A vertical load of approximately 150 kN was applied to the column, which corresponds to an axial load ratio of 0.22. The vertical load was kept practically constant during the test by means of a 250 kN actuator. This actuator was supported by two bolted steel bars, which were fixed to the foundation block. The axial vertical force was measured with a 500 kN load cell with 0.5% accuracy (cell C2 in Fig. 1). Linear variable displacement transducers (LVDT) were used to record the horizontal displacements of the column, as well as an eventual vertical movement of the footing (see Fig. 2). The measuring stroke for each LVDT is indicated in parentheses (±12.5 or ±25 mm). The location of the strain-gauges (SG) which were glued to the CFRP strips is also indicated in Fig. 2.

The tests were carried out with closed-loop servo-controlled equipment. A displacement history was imposed to LVDT1, with

Table 1
Denominations for the specimens

Longitudinal reinforcement (1)	Series		
	NON[a] (2)	PRE[b] (3)	POS[c] (4)
4ϕ10	C10a_NON	C10a_PRE	C10a_POS
	C10b_NON	C10b_PRE	C10b_POS
4ϕ12	C12a_NON	C12a_PRE	C12a_POS
	C12b_NON	C12b_PRE	C12b_POS

[a] Non-strengthened.
[b] Strengthened before testing.
[c] Columns of NON series after have been tested and strengthened.

Table 2
Maximum forces obtained in the columns of PRE series (strengthened before testing)

	Series PRE			
	C10a_PRE	C10b_PRE	C12a_PRE	C12b_PRE
Age[a] (days)	111	113	110	115
Average compressive strength[a] (MPa)	17.49	14.99	23.55	17.93
Tensile (kN)	37.14	40.63	44.13	39.81
Compressive (kN)	−38.54	−37.96	−43.66	−36.64

[a] Values at the age of the columns at testing.

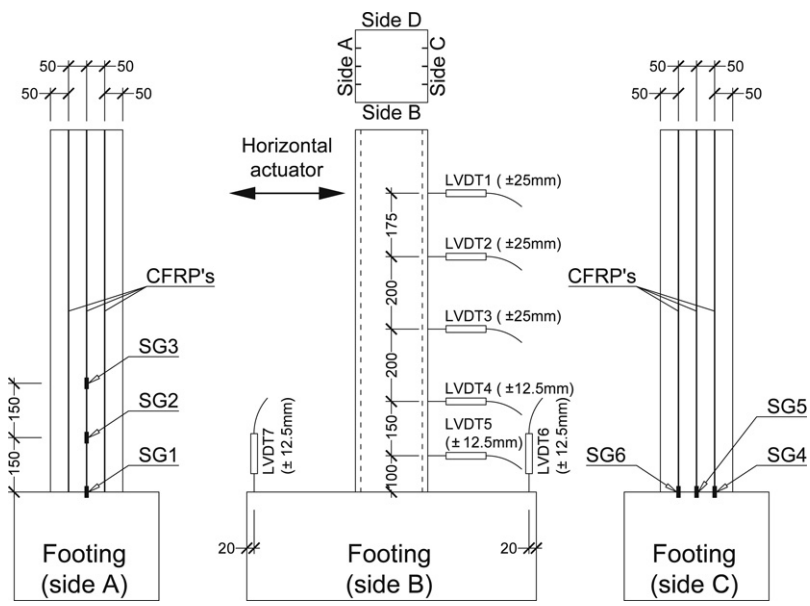

Fig. 2. Location of the displacement transducers (LVDT) and strain gauges (SG) (dimensions in mm).

a full range of 50 mm and 0.05% accuracy, located at the level of the horizontal actuator, see Fig. 1 and Fig. 2. From the analytical and numerical simulations it was verified that the steel yield initiation occurred for a lateral deflection of about 5 mm at the level of the horizontal actuator. Therefore, an increment of 2.5 mm was selected in the present experimental program. This increment was the same for all the specimens, in order to allow for the comparison of stiffness and strength degradation for the same lateral deflections. The displacement history included eight full loading-unloading cycles: ±2.5 mm, ±5.0 mm, ±7.5 mm, ±10.0 mm, ±12.5 mm, ±15.0 mm, ±17.5 mm and ±20.0 mm, with a displacement rate of 150 μm/s.

4. Material characterization

4.1. Concrete

A low strength concrete was used for all tests, in order to reproduce the type of concrete used in the sixties and seventies. The concrete was composed of 250 kg/m^3 of normal Portland cement, 1196.5 kg/m^3 of gravel 5–15 mm, 797.5 kg/m^3 of sand 0–5 mm, and 151.5 l/m^3 of water.

The uniaxial compressive behaviour of the concrete of each column series was assessed by performing compression tests with two cylinders of 150 mm diameter and 300 mm height. These tests were performed at 28 days and at the time the columns were tested. For each series of columns, two beams with dimensions of 850 × 100 × 100 mm^3 were also cast for assessing the tensile strength in bending and the fracture energy of the concrete [14]. The results obtained in the compression tests indicated an average compressive strength, at 28 days, of 16.7 MPa, with a standard deviation of 3.31 MPa. An average tensile strength of 2.62 MPa, with a standard deviation of 0.48 MPa, and an average fracture energy of 0.08 N mm/mm^2 were registered from the three-point notched beam bending tests, at 28 days. Tables 2 and 3 include the values of the concrete compressive strength at the age of the column tests.

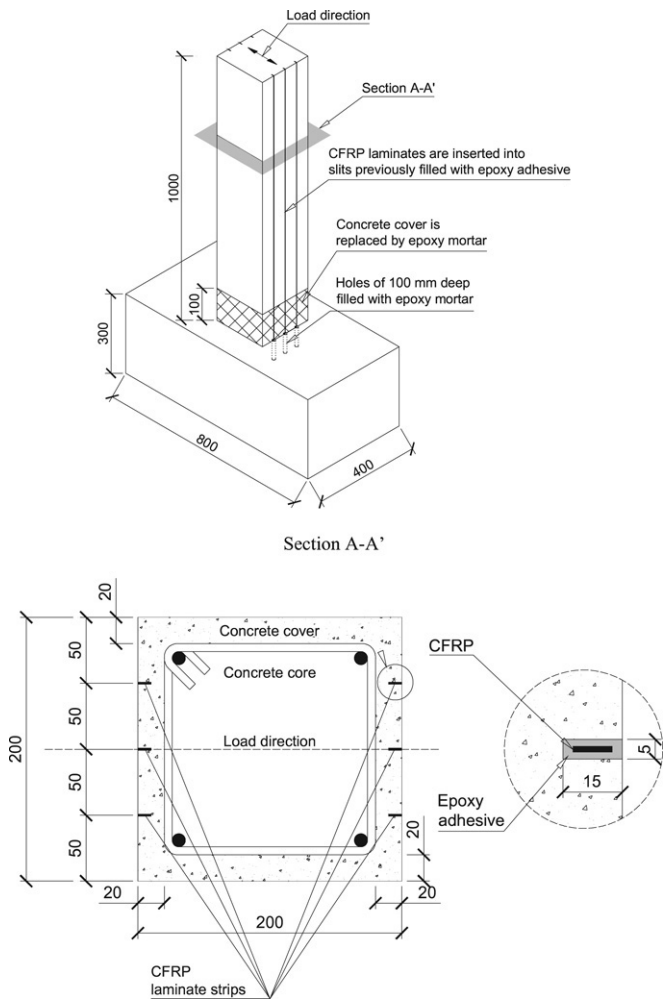

Fig. 3. Adopted flexural strengthening technique for RC columns (dimensions in mm).

4.2. Steel reinforcement

In the RC structures built in the sixties and seventies smooth surface steel bars were commonly used. For this reason, this type of bars was also used in the reinforcement of the tested columns. To assess the behaviour of the steel bars, uniaxial tensile tests were carried out in a servo-controlled testing machine, according to the recommendations of the European standard EN 10 002 [15]. The yield stress (f_{sy}), the ultimate stress (f_{su}), and the elasticity modulus (E_s) of $\phi 6$ bars are (as an average of the tests with three specimens): $f_{sy} = 352.4$ MPa, $f_{su} = 352.8$ MPa, and $E_s = 203\,700$ MPa. The reinforcement details for $\phi 10$ and $\phi 12$ bars are presented later (see Table 6).

Table 3
Maximum forces obtained on the columns of series NON (non-strengthened) and POS (strengthened after preliminary testing)

Column		C10a_	C10b_	C12a_	C12b_
Diameter of longitudinal bars (mm)		10	10	12	12
Average compressive strength[a] (MPa)		15.21	13.21	17.23	19.95
Tensile	NON (kN)	16.67 (86)[b]	21.78 (85)[b]	26.35 (85)[b]	29.31 (85)[b]
	POS (kN)	37.96 (146)[b]	41.38 (130)[b]	34.11 (150)[b]	45.54 (154)[b]
	Increase (%)	127.7	89.99	29.45	55.37
Compressive	NON (kN)	−19.76 (86)[b]	−24.07 (85)[b]	−30.52 (85)[b]	−32.27 (85)[b]
	POS (kN)	−34.11 (146)[b]	−43.1 (130)[b]	−37.03 (150)[b]	−41.58 (154)[b]
	Increase (%)	72.62	79.06	21.33	28.85

[a] Values at the age of the columns at testing of the series NON.
[b] Values inside round parentheses represent the age of the columns at testing, in days.

4.3. Epoxy mortar

An epoxy mortar was used to fix the CFRP laminates to the column footing (see Fig. 3). The epoxy mortar was composed of one part of epoxy and three parts of fine sand previously washed and dried (parts measured in weight). The uniaxial compressive strength and the flexural tensile strength of the epoxy mortar were evaluated from tests in specimens with $160 \times 40 \times 40$ mm^3, at 48 h and at 28 days, following the European standard [16]. At 48 hours, a compressive strength of 43.75 MPa, with a standard deviation of 2.14 MPa, and a flexural tensile strength of 33.93 MPa with a standard deviation of 0.57 MPa, were obtained. At 28 days, a compressive strength of 51.71 MPa, with a standard deviation of 0.47 MPa, and a flexural tensile strength of 35.40 MPa, with a standard deviation of 1.70 MPa, were obtained.

In order to evaluate the adhesive properties of the epoxy mortar relatively to a concrete surface, the following procedure was undertaken: reutilization of the remains of previous bending tests with $850 \times 100 \times 100$ mm^3 beams, which were used to evaluate the properties of the concrete used in the columns; utilization of the epoxy mortar to glue both pieces together; test of the resulting specimen under flexure load. In these tests it could be observed that the fracture neither propagated across the epoxy mortar, nor across its interface with the concrete (see Fig. 4). Therefore, these tests indicated that the properties of the bonding between the developed epoxy mortar and concrete are very good.

4.4. CFRP laminate strips

The CFRP strips, which were provided in rolls, had a thickness of 1.45 ± 0.005 mm and a width of 9.59 ± 0.09 mm (average values of 15 measures). To evaluate the tensile strength and the elasticity

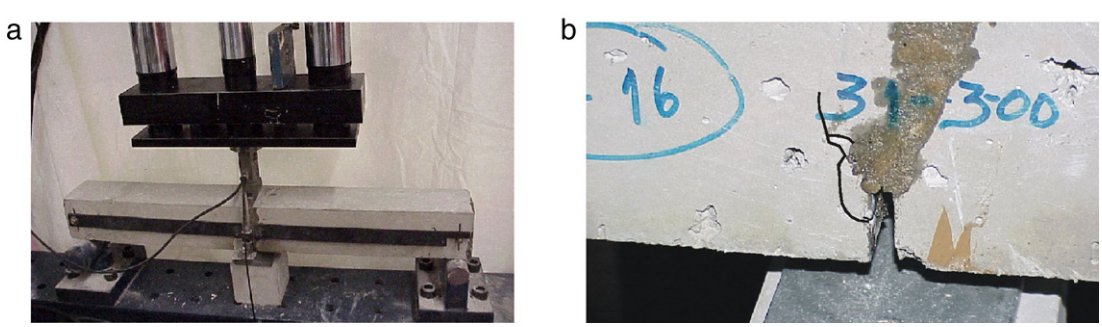

Fig. 4. Notched beam bending tests for the characterization of the concrete-epoxy mortar bond performance: (a) test setup; (b) crack propagation.

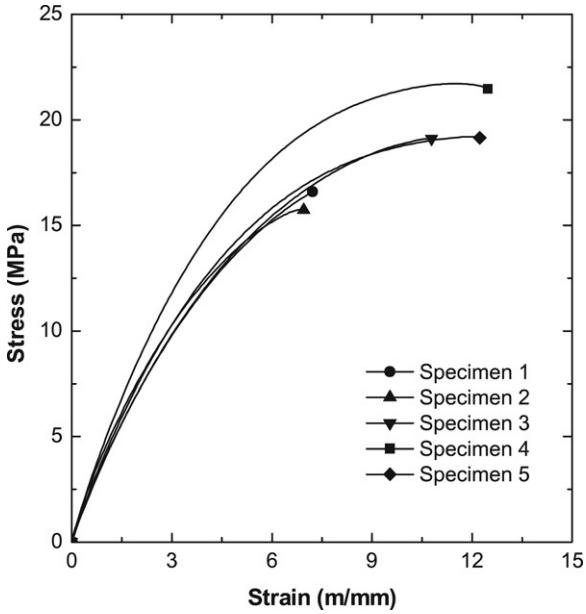

Fig. 5. Tensile stress–strain relationship for the epoxy adhesive specimens.

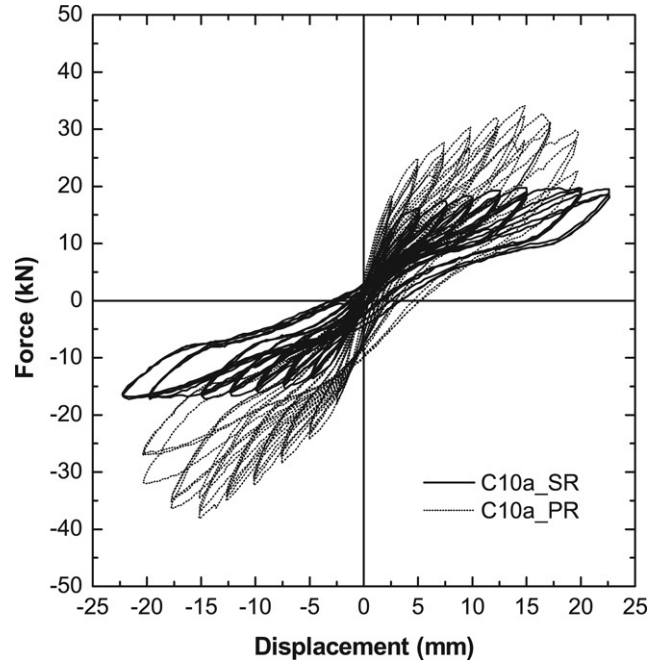

Fig. 6. Cyclic force–deflection (at LVDT1) relationship for C10a column.

modulus of the applied strips, uniaxial tensile tests were carried out in a servo-controlled test machine (Instron, series 4208), according to the recommendations of ISO 527-5 [17]. Strains were registered by means of a clip-gauge with a measuring stroke of 50 mm, whereas forces were obtained from a 100 kN load cell with an accuracy less than 0.1%. The stress–strain relationships obtained were linear up to failure, which indicates a brittle behaviour. An elasticity modulus of 159 000 MPa and a tensile strength of 1741 MPa resulted from the tests.

4.5. Epoxy adhesive

The adhesive that was used to bond the CFRP strips to concrete was composed of two parts of epoxy and one part of a hardening component (parts measured in weight). In order to assess the tensile behaviour of the epoxy adhesive, five specimens were tested with the same equipment and measurement devices that were used in the uniaxial tensile tests of the CFRP strips (see the previous Section). The tests were carried out according to the recommendations of ISO 527-2 [18] and a load cell with 5 kN load capacity was used. Fig. 5 shows the uniaxial stress–strain curves obtained in the tests. All the specimens exhibited similar uniaxial stress–strain relationships with the exception of the fourth. However, significant differences are observed in terms of tensile strength probably due to spurious voids detected in the fracture surfaces of the tested specimens. In fact, in the fracture surface of specimen 4 the imperfections were all micro-voids, while in the other specimens voids of a considerably larger size were observed. According to the recommendations of ISO 527-2 [18], an elasticity modulus of 5090 $\pm$ 590 MPa was obtained.

5. Adopted strengthening technique

Fig. 3 presents the strengthening technique adopted for the column elements. In a region 100–150 mm high at the bottom of the column (herein designated as "nonlinear hinged region") the concrete cover was removed. Afterwards, 5 mm wide and 15 mm deep slits were cut in the concrete cover, in the faces that will be subjected to the highest tensile stresses. In order to anchor the CFRP strips to the footing, 100 mm deep perforations were made in correspondence with each slit. Before the installation of the strips, all the slits and holes were cleaned using steel brushes and compressed air. The CFRP strips were cleaned with a solvent. The slits were then filled with the epoxy adhesive and the strips were installed into the slits. Finally, the nonlinear hinged region and the holes in the footing were filled with the epoxy mortar. A detailed description of this strengthening technique can be found in [19].

6. Experimental results

6.1. Load carrying capacity

The test series was carried out with the procedures described in Section 3. Tables 2 and 3 contain the extreme values obtained in the tests for the horizontal force considering as positive a right to left force in Fig. 1 (the age of the columns at testing time is in parentheses). The maximum force observed differs significantly, even between specimens of the same series. This discrepancy is mainly due to the variability of the concrete properties and to some extent lack of precision in the location of the steel reinforcement. A significant increase of the maximum load of the columns of the PRE series (strengthened before testing) and POS series (strengthened after testing) was observed, relatively to the results obtained in the columns of the NON series. As expected, the strength increase provided by the CFRP was higher in the columns with lower longitudinal steel reinforcement ratios (C10 series). The increase of the load carrying capacity provided by the NSM strengthening technique was similar in the PRE series and in previously tested columns (POS series).

6.2. Force–displacement relationships

Fig. 6 shows two typical relationships between the horizontal force and the deflection at LVDT1. The envelopes of the relationships between force and deflection at LVDT1 for all the tested columns are shown in Figs. 7 to 9. It can be observed that, in columns reinforced with ϕ10 and ϕ12 bars, the increase of the load carrying capacity occurred before and after yielding of the steel longitudinal reinforcement, respectively. Up to a deflection that approximately corresponds to the yield initiation of the steel

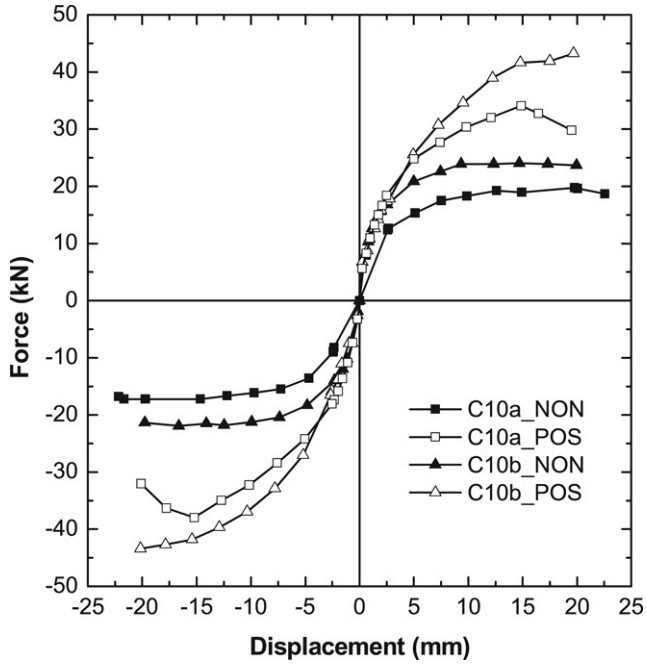

Fig. 7. Force–displacement envelopes for all load cycles of series C10_NON and C10_POS.

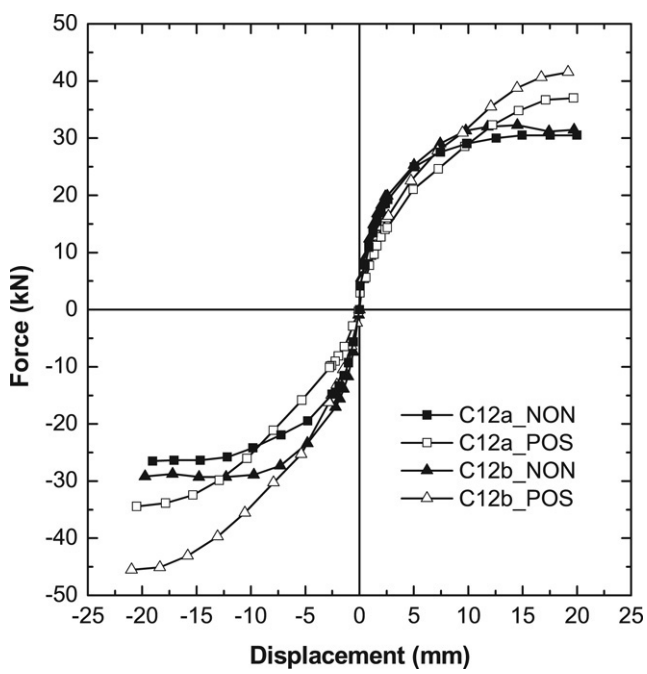

Fig. 8. Force–displacement envelopes for all load cycles of series C12_NON and C12_POS.

longitudinal reinforcement, the stiffness of the columns of the POS series was, in general, lower than the stiffness of the columns of PRE and NON series, since, when tested, the columns of the POS series were already significantly damaged. This effect is more evident in the columns possessing more longitudinal reinforcement, since, due to the higher maximum load applied to these columns, the concrete was significantly more damaged. In general, a pronounced pinching effect occurred (narrowing of the hysteretic diagrams), indicating that these columns had reduced capacity to dissipate energy. The relative high concrete compressive axial stress (3.75 MPa) and the low concrete compressive strength class applied in the tested columns have contributed to this behaviour.

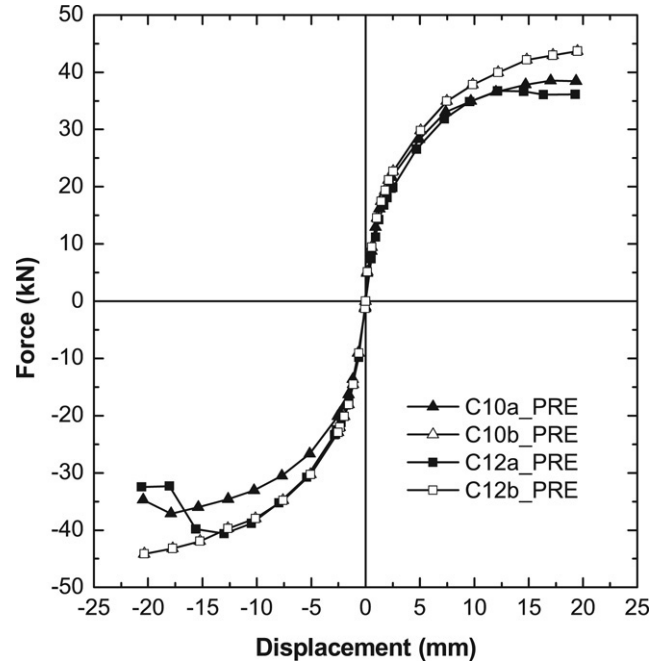

Fig. 9. Force–displacement envelopes for all load cycles of series PRE.

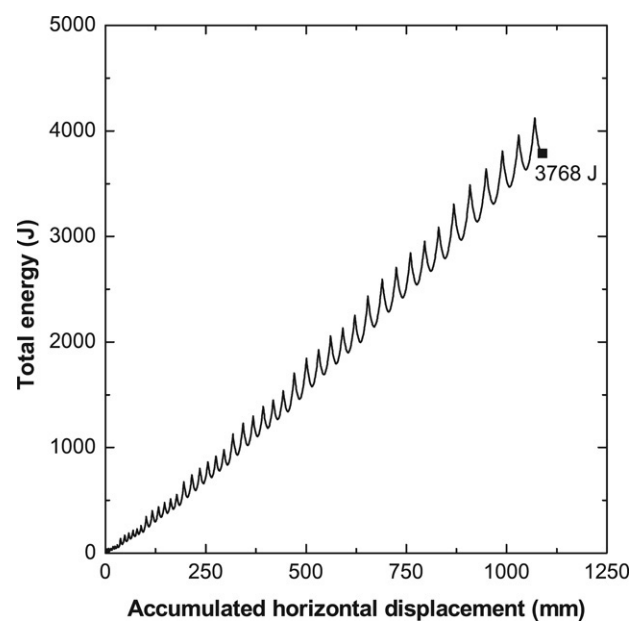

Fig. 10. Total energy *vs.* accumulated horizontal displacement for C12b_POS column.

In the strengthened columns this pinching effect was even more pronounced since, due to the increase of the flexural carrying capacity provided by the CFRP strips, the concrete axial compressive stresses have increased. From the horizontal force *vs.* deflection at LVDT1 relationships recorded in the cyclic tests, the following diagrams can be obtained: dissipated energy *vs.* accumulated horizontal displacement, and maximum horizontal force in each series of load cycles *vs.* horizontal displacement. Typical graphs for these relationships are depicted in Figs. 10 and 11, which correspond to the C12b_POS column. Due to the fact that this strengthening technique does not provide significant concrete confinement, the increase on the dissipated energy was marginal. Table 4 includes the values of the dissipated energy obtained in the cyclic tests.

Table 4
Dissipated energy

Column reference	Accumulated horizontal displacement (mm)	Dissipated energy (kN mm)
C10a_NON	1139	2013
C10a_POS	1081	3457 (72%)
C10a_PRE	1081	3732
C10b_NON	1083	2627
C10b_POS	1090	3786 (44%)
C10b_PRE	1082	3436
C12a_NON	1078	2552
C12a_POS	1089	3216 (26%)
C12a_PRE	1082	3436
C12b_NON	1077	3344
C12b_POS	1094	3777 (13%)
C12b_PRE	1090	3560

Values inside parentheses represent the dissipated energy increment.

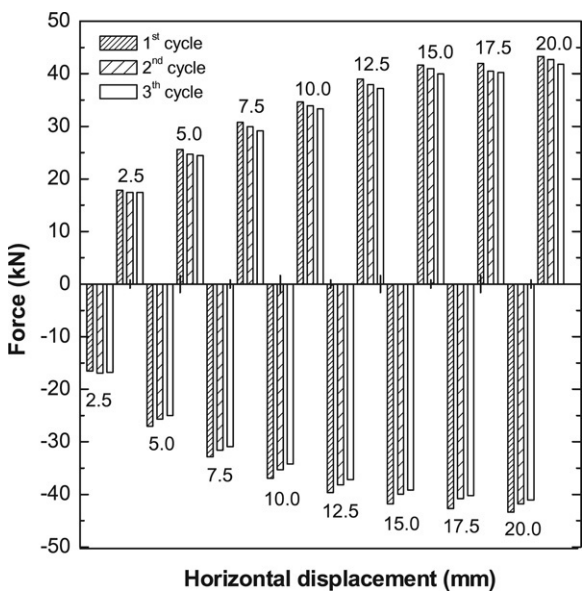

Fig. 11. Variation of the peak load in the load cycles for C12b_POS column.

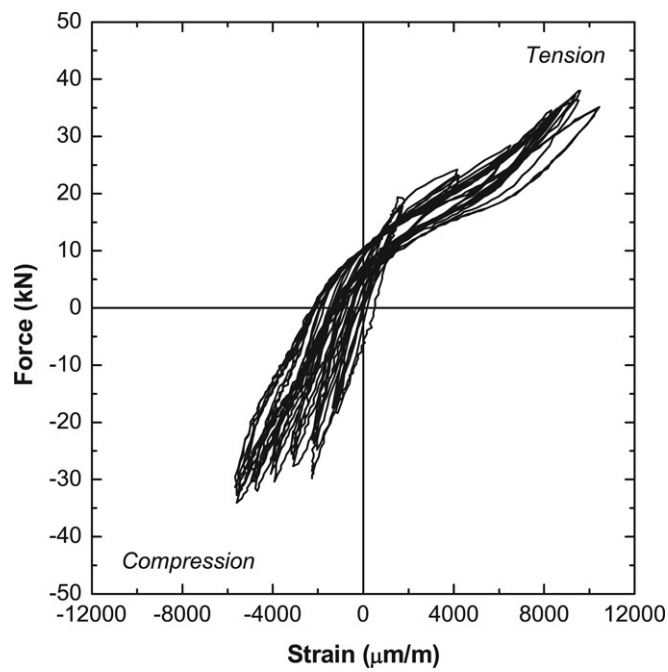

Fig. 12. Relationship between the force and the strain on the strain gauge SG6 (see Fig. 2) for the column C10a_POS.

6.3. Force–strain relationships

In the majority of the strengthened columns some CFRP strips have reached tensile strain values close to their ultimate strain (≅1%). As an example, Fig. 12 illustrates, for the column C10a_POS, the relationship between the horizontal force applied to the column and the strain measured in the *SG6* strain-gauge (see also Fig. 2). Due to the contribution of the surrounding concrete, the maximum compressive strain in the CFRP was about half the value recorded in tension. Relationships similar to those depicted in Fig. 12 were obtained for the remaining columns.

6.4. Crack patterns and failure modes

In all the tested columns a flexural failure mode occurred. Fig. 13 shows the crack patterns that could be observed in the four lateral faces the columns C10a_NON and C10a_POS, according to the labels indicated in Fig. 2. These crack patterns are representative of the NON and POS series of columns. The crack patterns of the PRE and POS series of columns are similar (see also [19]). Fig. 13 shows that in the NON columns the flexural failure crack formed at the column-footing interface, while in the PRE and POS columns a more diffuse crack pattern occurred. In these cases the flexural failure crack is located above the repaired zone, i.e. approximately 150 mm above the column bottom surface. This new location of the failure surface contributed to the increase of the flexural load carrying capacity of the strengthened columns.

7. Numerical simulation

7.1. Introduction

A fibrous model with cyclic constitutive laws for concrete and steel bars was implemented in the FEMIX computer program [20], which is based on the finite element method. The fibrous model was incorporated in the three-dimensional Timoshenko beam finite element [12]. With this finite element and the FEMIX framework, three-dimensional reinforced concrete frames with cyclic loading and nonlinear material behaviour can be analysed. This model was used in the numerical simulation of the behaviour of RC columns strengthened with the NSM technique and submitted to axial and cyclic lateral loads (see the previous Sections). The simulated columns were discretized with isoparametric Timoshenko beam elements with three nodes each. The cross section of each element is discretized with 4-noded quadrilateral elements representing each a longitudinal fibre (see Fig. 14). The geometry of the cross section of each fibre can vary along the beam element. The material model may vary from fibre to fibre thus allowing for the consideration of non constant concrete properties in the cross section (e.g., unconfined and confined concrete). A 2×2 Gauss–Legendre rule is adopted to

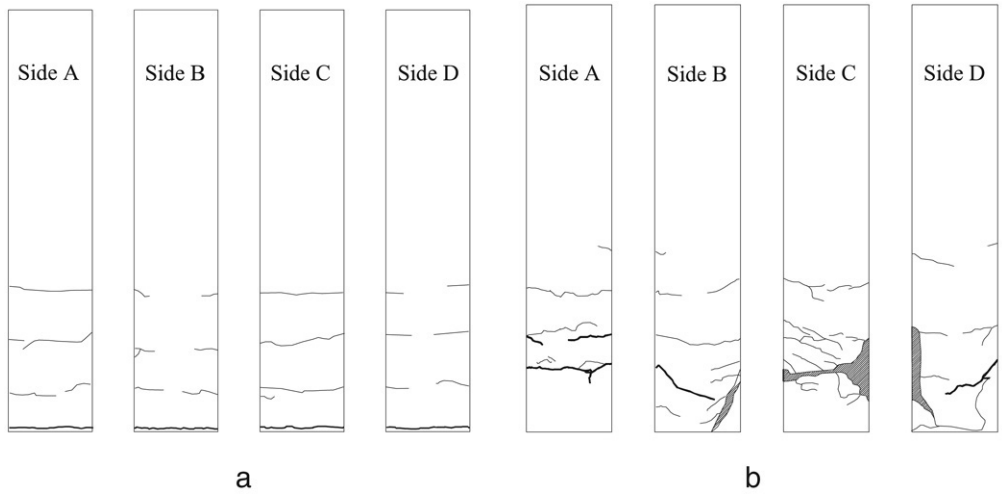

Fig. 13. Crack pattern on column C10a_NON (a) and C10a_POS (b) Note: thick line means higher crack opening; shaded zone represents concrete too damaged.

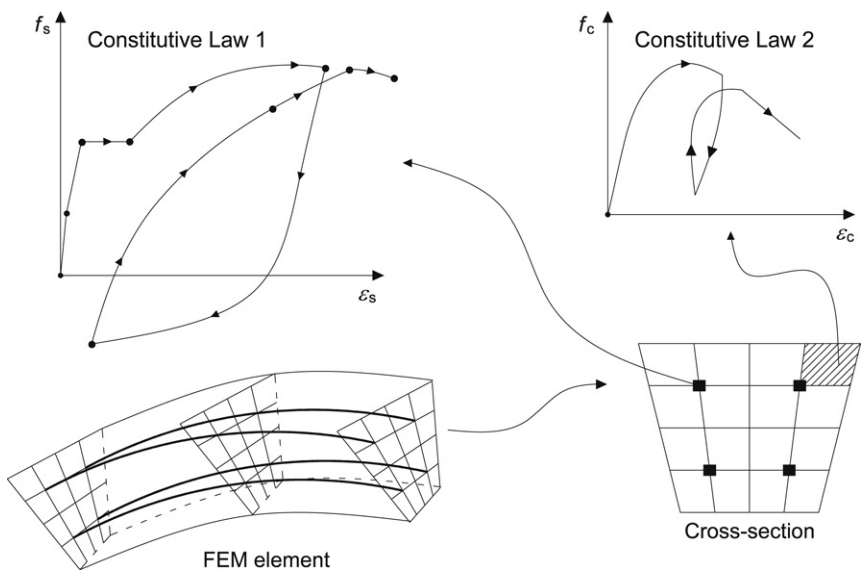

Fig. 14. Fibrous model concept.

evaluate the integrals related to each 4-noded finite element used in the discretization of the cross section. In the integrals that are required to evaluate the stiffness matrix and the internal forces of the Timoshenko beam element a Gauss–Legendre rule with two points is used. A linear stress–strain relationship was assumed for the CFRP strips, in agreement with the results obtained in the experimental tests. The formulation that was adopted for the simulation of the cyclic behaviour of the concrete and steel materials is briefly described in the following sections. A more detailed description can be found elsewhere [21,22].

7.2. Constitutive laws

7.2.1. Concrete cyclic model

Chang and Mander [21] developed a cyclic model for unconfined and confined concrete based on the expression that was originally proposed by Tsai [23] to simulate the monotonic concrete compressive behaviour. Chang and Mander assumed that concrete subjected to a monotonic tensile stress can also be simulated with the Tsai equation by selecting appropriate values for the parameters.

In the present work the aforementioned models are adopted, with minor adjustments, to simulate the concrete behaviour under monotonic and cyclic loading. These adjustments essentially involve the calculation procedure of parameter r in Eq. (3) (see Appendix A). The new procedure is based on experimental results that suggest the calculation of the parameter r with Eq. (4).

7.2.2. Steel cyclic model

The original formulation of the Menegotto and Pinto model is adopted in the present work [24]. A brief description of this model is included in Appendix B. Some adjustments are necessary, being the main modification restricted to Eq. (22).

8. Model appraisal

The tested RC columns were numerically simulated with the FEMIX computer code [20]. All the tested columns were discretized with six isoparametric Timoshenko beam elements with three nodes each. According to the developed approach, at the cross section level each fibre is discretized with a quadrilateral finite element. These fibres are represented by 4-noded finite elements with a 2×2 Gauss–Legendre integration rule, thus simulating the concrete core, concrete cover, steel bars and CFRP strips. The concrete part of the cross section was discretized with sixteen

Table 5
Data used in the numerical analysis to simulate the concrete behaviour

Column	f_{cc} (N/mm^2)	ε_{cc}	x_{cr}^-	E_c[a] (N/mm^2)	ε_{ct}	x_{cr}^+	f_{ct}[b] (N/mm^2)
C10b_NON	13.21	2.50e−3	2	20052	1.20e−4	2	1.20
C10b_PRE	14.79	2.50e−3	2	20821	1.40e−4	2	1.36
C12b_NON	19.95	2.50e−3	2	23000	2.50e−4	2	1.57
C12b_PRE	17.93	2.50e−3	2	22001	1.89e−4	2	1.42

[a] Young's Modulus.
[b] Uniaxial tensile strength, according to CEB–FIP Model Code [26].

Table 6
Data used in the numerical analysis to simulate the behaviour of the steel bars

Column	E_s (N/mm^2)	f_{sy} (N/mm^2)	ε_{sh}	f_{sh} (N/mm^2)	ε_{su}	f_{su} (N/mm^2)	E_{sh} (N/mm^2)
C10	216 900	323.3	0.0075	344.0	0.03	456.5	6400.0
C12	229 700	364.8	0.0035	384.0	0.03	518.8	6400.0

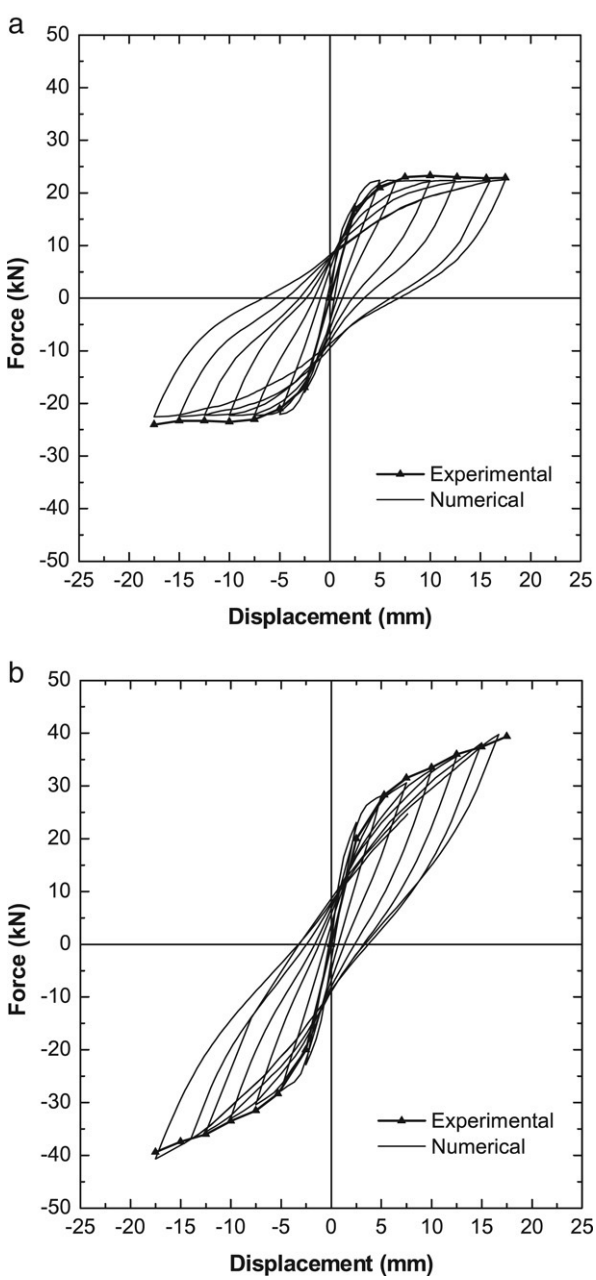

Fig. 15. Numerical and experimental results of the (a) C10b_NON and (b) C10b_PRE columns.

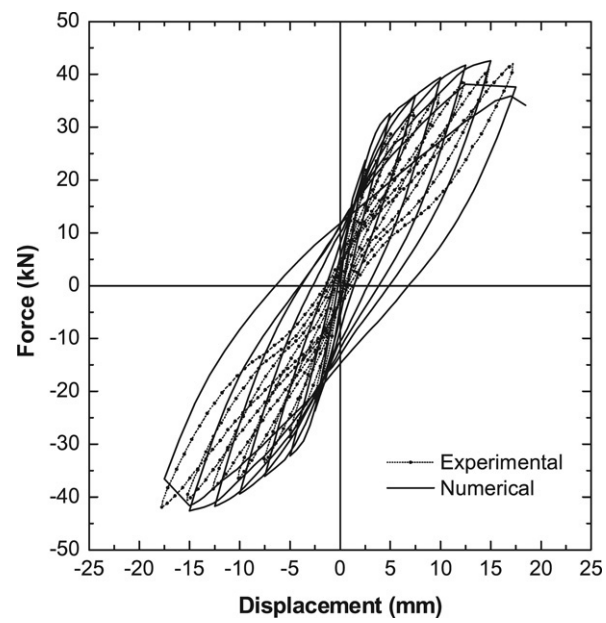

Fig. 16. Numerical and experimental results of the C12b_PRE column.

quadrilateral elements. Each longitudinal bar and each CFRP strip was simulated with an additional quadrilateral element. A linear stress–strain relationship was assumed for the CFRP strips, in agreement with the results obtained in the experimental tests [19]. Tables 5 and 6 include the values that were adopted for the parameters that define the concrete and steel constitutive models (the definition of the parameters included in these tables can be found in Appendices A and B). These values were obtained from tests that were carried out with concrete and steel specimens, as described in Section 4.

Fig. 15 shows the comparison between the experimental and numerical envelope curves for the NON and PRE tested columns with $\phi 10$ steel bars. It can be concluded that the implemented numerical model reproduces the main phenomena observed in the experimental tests.

The POS columns require a two-phase structural analysis: without and with strengthening. Since the computer code cannot simulate a structure with more than one phase, the POS columns were not numerically analyzed.

Fig. 16 includes, for the C12b_PRE column, the numerical and experimental horizontal force-deflection relationships. Regardless of correctly predicting the envelope response, in the numerical model larger energy dissipation occurred when compared with the experimental test. This is due to the fact that, in the present version of the program, it was assumed that concrete behaves

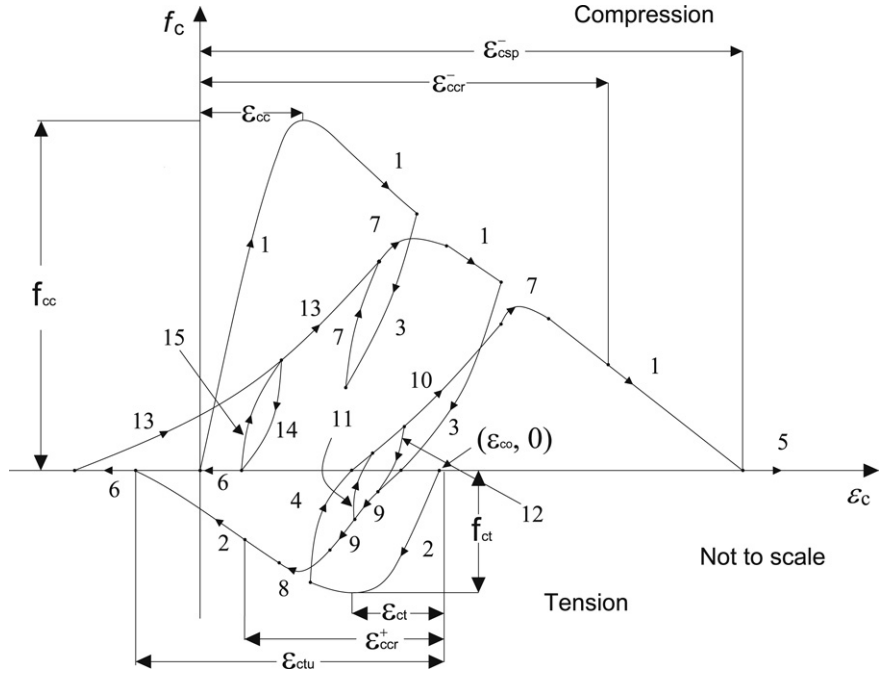

Fig. 17. Schematic representation of the concrete cyclic constitutive model.

linear-elastically in shear, which is an inaccurate approach, and the inelastic buckling of the steel bars was not integrated in the steel cyclic constitutive model. The incapability of the numerical model to simulate the pronounced pinching effect observed in the experimental tests resides on the fact that the model, in the present version, can not model the debonding between reinforcement and surrounding concrete, which results in a reduction of the energy dissipation capacity of the RC column. To accurately simulate this effect, a bond-slip model needs to be implemented to model the bond behaviour between reinforcement and concrete.

9. Conclusions

A strengthening technique based on bonding CFRP laminate strips into slits opened on the concrete cover was applied to RC columns subjected to axial compression and lateral cyclic loading. Since the amount of CFRP strengthening was the same for all columns, those with a smaller conventional steel reinforcement ($4\phi 10$) had a larger load carrying capacity increase (92%) than those with $4\phi 12$, which had only a capacity increase of 34%. With the proposed strengthening technique premature debonding could be avoided, which allowed for the possibility of a full exploitation of the CFRP resistance as was indicated by the attainment of high strain values. This fact lead to the failure of some CFRP strips in the base of the columns.

The obtained experimental results indicate that the proposed strengthening technique is very promising for increasing the load carrying capacity of concrete columns failing in bending. However, as was expected, the energy absorption capacity of the tested RC columns was not improved by this technique, since it does not provide significant concrete confinement.

With the aim of simulating the behaviour of reinforced concrete columns strengthened with the technique proposed in this work, a fibrous model with cyclic constitutive laws for concrete and steel bars was implemented in a computational code based on finite element techniques. This computational model can simulate the cyclic behaviour in compression and in tension of unconfined and confined concrete. The numerical model has reproduced, with good agreement, the behaviour observed in the experiments, being a useful tool for the analysis of this type of structures.

Acknowledgments

The study reported in this paper is included in the research program "CUTINSHEAR—Performance assessment of an innovative structural FRP strengthening technique using an integrated system based on optical fiber sensors" supported by FCT, POCTI/ECM/59033/2004. The second author acknowledges the support provided by the grant in the ambit of this research project.

Appendix A. Chang and Mander model

Fig. 17 represents the envelope curves and cyclic rules of the model. The superscript + or − indicates that the parameter corresponds to a tensile or compressive state, respectively. The non-dimensional stress–strain relationship of the envelope curve for the case of the compressive behaviour can be written in the following manner:

$$\text{for } 0 < x_c^- < x_{ccr}^- \quad f_c^- = f_{cc} y(x_c^-) \quad E_{ct}^- = E_c z(x_c^-) \tag{1a}$$

$$\text{for } x_{ccr}^- \le x_c^- \le x_{csp} \quad f_c^- = f_{cc}[y(x_{ccr}^-) + n_c^- z(x_{ccr}^-)(x_c^- - x_{ccr}^-)] \quad E_{ccr}^- = E_c z(x_{ccr}^-) \tag{1b}$$

$$\text{for } x_c^- > x_{csp} \quad f_c^- = E_{ct}^- = 0 \tag{1c}$$

where, f_{cc} is the concrete compressive strength (for confined concrete $f_{cc} = f'_{cc}$; for unconfined concrete $f_{cc} = f'_c$), E_c is the concrete initial Young's Modulus (CEB-FIP 1993, [26]),

$$y(x_c) = \frac{n_c x_c}{D(x_c)} \tag{2}$$

$$z(x_c) = \frac{\left[1 - (x_c)^r\right]}{[D(x_c)]^2} \tag{3}$$

$$r = \frac{f_{cc}}{2.5} - 1.9, \quad \text{with } f_{cc} \text{ in MPa} \tag{4}$$

Table 7
Controlling parameters used in transition curves for the concrete cyclic constitutive model

Parameters	Rule number										
	3	4	7	8	9	10	11	12	13	14	15
ε_{ca}	$\varepsilon^-_{\text{cun}}$	$\varepsilon^+_{\text{cun}}$	$\varepsilon^-_{\text{cun}}$	$\varepsilon^+_{\text{cun}}$	$\varepsilon^-_{\text{cpl}}$	$\varepsilon^+_{\text{cpl}}$	ε_{cr}	ε_{cr}	ε_{cr}	ε_{cr}	ε_{cr}
f_{ca}	f^-_{cun}	f^+_{cun}	f^-_{cnew}	f^+_{cnew}	0	0	f_{cr}	f_{cr}	0	f_{cr}	f_{cr}
E_{ca}	E_c	E_c	E^-_{cnew}	E^+_{cnew}	E^-_{cpl}	E^+_{cpl}	E_c	E_c	0	E_c	E_c
ε_{cb}	$\varepsilon^-_{\text{cpl}}$	$\varepsilon^+_{\text{cpl}}$	$\varepsilon^-_{\text{cre}}$	$\varepsilon^+_{\text{cre}}$	$\varepsilon^+_{\text{cun}}$	$\varepsilon^-_{\text{cun}}$	ε_{cb}	ε_{ca}	$\varepsilon^-_{\text{cun}}$	ε_{cb}	ε_{ca}
f_{cb}	0	0	f^-_{cre}	f^+_{cre}	f^+_{cnew}	f^-_{cnew}	f_{cb}	f_{ca}	f^-_{cnew}	0	f_{ca}
E_{cb}	E^-_{cpl}	E^+_{cpl}	E^-_{cre}	E^+_{cre}	E^+_{cnew}	E^-_{cnew}	$E_{ct,9}(\varepsilon_b)$	$E_{ct,10}(\varepsilon_a)$	E^-_{cnew}	0	$E_{ct,13}(\varepsilon_a)$

Table 8
Parameters used in transition curves for the concrete cyclic constitutive model

Parameter	(−)	(+)	Parameter	(−)	(+)
$E^{\pm}_{c\,\text{sec}}$	$E_c\left(\dfrac{\left\lvert\frac{f^-_{\text{cun}}}{E_c\varepsilon_{cc}}\right\rvert+0.57}{\left\lvert\frac{\varepsilon^-_{\text{cun}}}{\varepsilon_{cc}}\right\rvert+0.57}\right)$	$E_c\left(\dfrac{\left\lvert\frac{f^+_{\text{cun}}}{E_c\varepsilon_{ct}}\right\rvert+0.67}{\left\lvert\frac{\varepsilon^+_{\text{cun}}-\varepsilon_{co}}{\varepsilon_{ct}}\right\rvert+0.67}\right)$	$\Delta\varepsilon^{\pm}_c$	$\dfrac{\varepsilon^-_{\text{cun}}}{1.15+2.75\left\lvert\frac{\varepsilon^-_{\text{cun}}}{\varepsilon_{cc}}\right\rvert}$	$0.22\varepsilon^+_{\text{cun}}$
$E^{\pm}_{\text{cpl}}$	$0.1E_c\exp\left(-2\left\lvert\frac{\varepsilon^-_{\text{cun}}}{\varepsilon_{cc}}\right\rvert\right)$	$\dfrac{E_c}{\left\lvert\frac{\varepsilon^+_{\text{cun}}-\varepsilon_{co}}{\varepsilon_{ct}}\right\rvert^{1.1}+1}$	$\Delta f^{\pm}_c$	$0.09f^-_{\text{cun}}\sqrt{\left\lvert\frac{\varepsilon^-_{\text{cun}}}{\varepsilon_{cc}}\right\rvert}$	$0.15f^+_{\text{cun}}$
$f^{\pm}_{\text{cnew}}$	$f^-_{\text{cun}}-\Delta f^-_c$	$f^+_{\text{cun}}-\Delta f^+_c$	$\varepsilon^{\pm}_{\text{cpl}}$	$\varepsilon^-_{\text{cun}}-\frac{f^-_{\text{cun}}}{E^-_{c\,\text{sec}}}$	$\varepsilon^+_{\text{cun}}-\frac{f^+_{\text{cun}}}{E^+_{c\,\text{sec}}}$
$E^{\pm}_{\text{cnew}}$	$\frac{f^-_{\text{cnew}}}{\varepsilon^-_{\text{cun}}-\varepsilon^-_{\text{cpl}}}$	$\frac{f^+_{\text{cnew}}}{\varepsilon^+_{\text{cun}}-\varepsilon^+_{\text{cpl}}}$	$\varepsilon^{\pm}_{\text{cre}}$	$\varepsilon^-_{\text{cun}}+\Delta\varepsilon^-_c$	$\varepsilon^+_{\text{cun}}+\Delta\varepsilon^+_c$
$f^{\pm}_{\text{cre}}$	$f^-_c\left(\left\lvert\frac{\varepsilon^-_{\text{cre}}}{\varepsilon_{cc}}\right\rvert\right)$	$f^+_c\left(\left\lvert\frac{\varepsilon^+_{\text{cre}}-\varepsilon_{co}}{\varepsilon_{ct}}\right\rvert\right)$	$E^{\pm}_{\text{cre}}$	$E^-_c\left(\left\lvert\frac{\varepsilon^-_{\text{cre}}}{\varepsilon_{cc}}\right\rvert\right)$	$E^+_c\left(\left\lvert\frac{\varepsilon^+_{\text{cre}}-\varepsilon_{co}}{\varepsilon_{ct}}\right\rvert\right)$

$f^-_{\text{cun}}=f^-_c\left(\frac{\varepsilon^-_{\text{cun}}}{\varepsilon_{cc}}\right); f^+_{\text{cun}}=f^+_c\left(\frac{\varepsilon^+_{\text{cun}}-\varepsilon_{co}}{\varepsilon_{ct}}\right)$.

$$\begin{aligned} D(x_c) &= 1+\left(n_c-\frac{r}{r-1}\right)x_c+\frac{(x_c)^r}{r-1} \quad \text{for } r\neq 1 \\ &= 1+[n_c-1+\ln(x_c)]\,x_c \quad \text{for } r=1. \end{aligned} \tag{5}$$

In the above equations x^-_c, x^-_{ccr} and n^-_c are defined by

$$x^-_c=\frac{\varepsilon_c}{\varepsilon_{cc}},\qquad x^-_{\text{ccr}}=\frac{\varepsilon_{\text{ccr}}}{\varepsilon_{cc}},\qquad n^-_c=\frac{E_c\varepsilon_{cc}}{f_{cc}}. \tag{6}$$

In (6) ε_{cc} is the strain that corresponds to the concrete compressive strength (for confined concrete $\varepsilon_{cc}=\varepsilon'_{cc}$; for unconfined concrete $\varepsilon_{cc}=\varepsilon'_c$, where ε'_{cc} and ε'_c are the strains that correspond to f'_{cc} and f'_c, respectively). The parameter ε_{ccr} represents the critical compressive strain, after which a linear stress–strain relationship is assumed for the concrete in compression (see Fig. 17).

The non-dimensional spalling strain, x_{csp}, determined according to Eq. (7), corresponds to the maximum compressive strain, after which, due to concrete spalling, it is assumed that the concrete residual strength is exhausted.

$$x_{\text{csp}}=x^-_{\text{ccr}}-\frac{y(x^-_{\text{ccr}})}{n^-_c z(x^-_{\text{ccr}})}. \tag{7}$$

Eqs. (1a) and (1b) define the rule 1, while Eq. (1c) defines the rule 5. As already mentioned, the shape of the tension envelope curve is the same as that of the compression envelope curve [21], hence similar Eqs. can be used to define the rule 2 (Eqs. (8a) and (8b)) and rule 6 Eq. (8c) of the concrete tension envelope curve, as follows:

$$\begin{aligned} &\text{for } x^+_c<x^+_{\text{ccr}} \\ &f^+_c=f_{ct}y(x^+_c) \\ &E^+_{ct}=E_c z(x^+_c) \end{aligned} \tag{8a}$$

$$\begin{aligned} &\text{for } x^+_{\text{ccr}}\le x^+_c\le x_{\text{ctu}} \\ &f^+_c=f_{ct}[y(x^+_{\text{ccr}})+n^+_c z(x^+_{\text{ccr}})(x^+_c-x^+_{\text{ccr}})] \\ &E^+_{\text{ccr}}=E_c z(x^+_{\text{ccr}}) \end{aligned} \tag{8b}$$

$$\begin{aligned} &\text{for } x^+_c>x_{\text{ctu}} \\ &f^+_c=E^+_{ct}=0 \end{aligned} \tag{8c}$$

where

$$\begin{aligned} &x^+_c=\left\lvert\frac{\varepsilon_c-\varepsilon_{co}}{\varepsilon_{ct}}\right\rvert,\qquad n^+_c=\frac{E_c\varepsilon_{ct}}{f_{ct}}\quad\text{and} \\ &x_{\text{ctu}}=x^+_{\text{ccr}}-\frac{y(x^+_{\text{ccr}})}{n^+_c z(x^+_{\text{ccr}})} \end{aligned} \tag{9}$$

with f_{ct} being the concrete tensile strength and ε_{ct} its corresponding strain. All other rules corresponding to unloading and reloading branches are represented by a transition curve, which starts from an already known starting point (a subscript a is used to designate this point: ε_{ca}; f_{ca}) and slope (E_{ca}) that needs to be evaluated, and ends at a target point (a subscript b is used to designate this point: ε_{cb}; f_{cb}), whose coordinates, as well as the slope at this point (E_{cb}) need to be calculated. The transition curve is represented by

$$f_c=f_{ca}+(\varepsilon_c-\varepsilon_{ca})\left(E_{ca}+A_c\,|\varepsilon_c-\varepsilon_{ca}|^{R_c}\right) \tag{10}$$

where

$$R_c=\frac{E_{cb}-E_{c\,\text{sec}}}{E_{c\,\text{sec}}-E_{ca}}\quad\text{and}\quad A_c=\frac{E_{c\,\text{sec}}-E_{ca}}{|\varepsilon_{cb}-\varepsilon_{ca}|^{R_c}}. \tag{11}$$

The rules are summarized in Table 7. The parameters used in this table are calculated using the expressions included in Table 8. In Table 7 ε_{cr} and f_{cr} are the strain and the stress components of the last reversal point. The parameter $E_{ct,k}(\varepsilon_{ci})$ in Table 7 represents the tangent Young's Modulus at strain ε_{ci} for the kth rule (i represents the a or b point). In Table 8 $f_c{}^{\pm}(\varepsilon_{ci})$ and $E_c{}^{\pm}(\varepsilon_{ci})$ represent the stress and the tangent elasticity modulus at strain ε_{ci}, evaluated with the equations that define the envelope curves.

If, during the unloading process modelled with rule 3, a reversal occurs (see Fig. 17), the values that define the target point of the function that establishes the rule 7 are obtained from linear interpolation, using values calculated with the expressions of Table 8 corresponding to rule 7, as described elsewhere [21].

Similarly, when a reversal in rule 4 takes place, a linear interpolation is used to obtain the values of the parameters that define the rule 8. A reversal in rule 9 is modelled with rule 11, while a reversal in rule 10 is simulated with rule 12 (see Fig. 17). In order to define the rules 11 and 12, the points a and b are

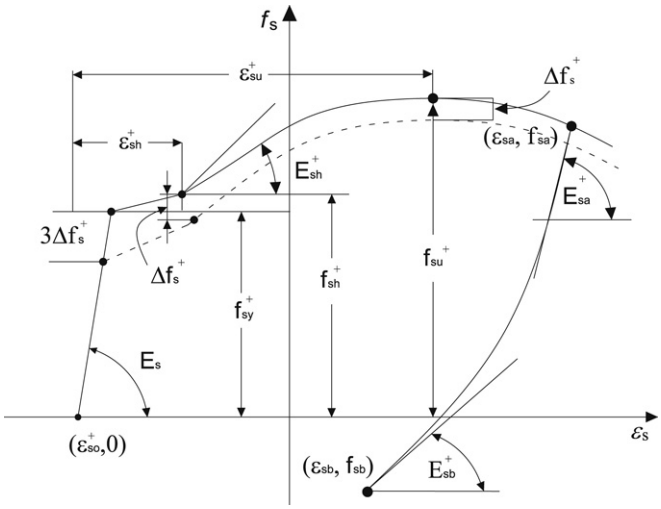

Fig. 18. Schematic representation of the parameters for the steel cyclic constitutive model.

assumed to be located in the branches corresponding to rule 9 and 10, respectively (in case of rule 12, *a* is now the target point). The following equation is used to obtain the strain at the target point

$$\frac{\varepsilon_{ca} - \varepsilon^-_{\text{cpl}}}{\varepsilon^+_{\text{cun}} - \varepsilon^-_{\text{cpl}}} = \frac{\varepsilon^-_{\text{cun}} - \varepsilon_{cb}}{\varepsilon^-_{\text{cun}} - \varepsilon^+_{\text{cpl}}}. \tag{12}$$

A reversal in rule 13 is simulated with rule 14, which has the *b* target point lying on the abscissa, whose strain value, ε_{cb}, can be calculated from the following equation

$$\varepsilon_{cb} = \varepsilon_{ca} - \frac{f_{ca}}{E^-_{c\,\text{sec}}}. \tag{13}$$

The shift in the tension envelope curve, whose definition is based on the strain parameter ε_{co} (see Fig. 17), is calculated as described in the following steps:

(a) Calculate the compressive and tensile non-dimensional strain ductility parameters

$$x^-_{cu} = \left|\frac{\varepsilon^-_{\text{cun}}}{\varepsilon_{cc}}\right| \quad \text{and} \quad x^+_{cu} = \left|\frac{\varepsilon^+_{\text{cun}} - \varepsilon_{co}}{\varepsilon_{ct}}\right|. \tag{14}$$

(Note: in the first iteration $\varepsilon_{co} = 0$; in the first reversal $\varepsilon^+_{\text{cun}} = 0$).

(b) If $x^+_{cu} < x^-_{cu}$ then

$$x^+_{cu} = x^-_{cu}, \qquad \varepsilon_{co} = 0, \qquad \varepsilon^+_{\text{cun}} = x^+_{cu}\varepsilon_{ct} \tag{15}$$

and the corresponding stress, f^+_{cun}, is obtained from the tensile envelope curve at $\varepsilon^+_{\text{cun}}$. The shift is finally calculated from

$$\varepsilon_{co} = \varepsilon^-_{\text{cpl}} + \Delta\varepsilon_{co} - x^+_{cu}\varepsilon_{ct}, \quad \text{where}, \Delta\varepsilon_{co} = \frac{2f^+_{\text{cun}}}{E^+_{c\,\text{sec}} + E^-_{\text{cpl}}}. \tag{16}$$

The utilization of the cyclic concrete model that was described above only requires the following parameters: E_c, f_{cc}, f_{ct}, ε_{cc}, ε_{ct}, $\varepsilon^+_{\text{ccr}}$, $\varepsilon^-_{\text{ccr}}$.

Appendix B. Menegotto and Pinto model

Ten rules define the cyclic model assumed for steel bars, being five associated with the compressive state and the remaining with the tensile state. The tensile and compressive envelope curves depend on the monotonic stress–strain (f_s–ε_s) relations defined by rules 1 and 2, respectively (see Figs. 18 and 19). The strain parameter ε_{so} (Fig. 18), which is dependent on the experienced plastic excursion into the envelope curve, can be relocated and scaled in order to simulate strength degradation [21].

The stress and the tangent elasticity modulus of the envelope curve are calculated with the expressions defined by Eqs. (17a) and (17b). In the following equations the tensile envelope curve (rule 1) is described by considering the (+) version of the parameters, while the compressive envelope curve (rule 2) by considering the (−) version.

$$f_s = \frac{E_s\varepsilon_{ss}}{\left[1 + \left(\frac{E_s\varepsilon_{ss}}{f^\pm_{sy}}\right)^{10}\right]^{0.1}} + \frac{\text{sign}\,(\Delta\varepsilon_{s1}) + 1}{2}(f^\pm_{su} - f^\pm_{sy}) \times \left(1 - \left|\frac{\varepsilon^\pm_{su} - \varepsilon_{ss}}{\varepsilon^\pm_{su} - \varepsilon^\pm_{sh}}\right|^{p\pm}\right) \tag{17a}$$

$$E_{st} = \frac{E_s}{\left[1 + \left(\frac{E_s\varepsilon_{ss}}{f^\pm_{sy}}\right)^{10}\right]^{1.1}} + \frac{\text{sign}\,(\Delta\varepsilon_{s1}) + 1}{2}\text{sign}\,(\Delta\varepsilon_{s2})E^\pm_{sh} \times \left|\frac{f^\pm_{su} - f_s}{f^\pm_{su} - f^\pm_{sy}}\right|^{\frac{p^\pm - 1}{p^\pm}} \tag{17b}$$

where

$$\varepsilon_{ss} = \varepsilon_s - \varepsilon^\pm_{so}; \qquad p^\pm = E^\pm_{sh}\frac{\varepsilon^\pm_{su} - \varepsilon^\pm_{sh}}{f^\pm_{su} - f^\pm_{sy}} \tag{18}$$

$$\Delta\varepsilon_{s1} = \varepsilon_{ss} - \varepsilon^+_{sh}; \qquad \Delta\varepsilon_{s2} = \varepsilon^+_{su} - \varepsilon_{ss}$$

for the case of the tensile envelope (19a)

$$\Delta\varepsilon_{s1} = \varepsilon^-_{sh} - \varepsilon_{ss}; \qquad \Delta\varepsilon_{s2} = \varepsilon_{ss} - \varepsilon^-_{su}$$

for the case of the compressive envelope. (19b)

All the rules simulating the unloading and reloading branches (see Fig. 19) are based on the model proposed by Menegotto and Pinto [24]. The following equations define these branches

$$f_s = f_{sa} + E_{sa}(\varepsilon_s - \varepsilon_{sa})\left(Q + \frac{1 - Q}{A}\right) \tag{20a}$$

$$E_{st} = E_{s\,\text{sec}} - \frac{E_{s\,\text{sec}} - QE_{sa}}{1 + \left|E_{sa}\frac{\varepsilon_s - \varepsilon_{sa}}{f_{ch} - f_{sa}}\right|^{-R_s}} \tag{20b}$$

where ε_{sa} and f_{sa} are the strain and stress components of the *a* initial point, E_{sa} is the tangent elasticity modulus at this point, and

$$A = \frac{1}{c} = \left[1 + \left|E_{sa}\frac{\varepsilon_s - \varepsilon_{sa}}{f_{ch} - f_{sa}}\right|^{R_s}\right]^{\frac{1}{R_s}}$$
$$Q = \frac{\frac{E_{s\,\text{sec}}}{E_{sa}} - c}{1 - c} \tag{21}$$
$$f_{ch} = f_{sa} + \frac{E_{sa}c}{(1 - c^{R_s})^{\frac{1}{R_s}}}(\varepsilon_{sb} - \varepsilon_{sa}).$$

An iterative procedure is required to obtain the strain and stress components that define the unloading and reloading branches. The parameters that define these rules are summarized in Table 9, where ε_{sr} and f_{sr} are the strain and the stress components of the last reversal point, and $\varepsilon_{s\,\max}$ and $\varepsilon_{s\,\min}$ are the maximum excursions into the tensile envelope branch and into the compressive envelope branch, respectively. Table 10 shows how to calculate the parameters required by the rules indicated in Table 9.

In a cracked reinforced concrete element the stress in the steel reinforcement attains a higher value in the vicinity of the cracks

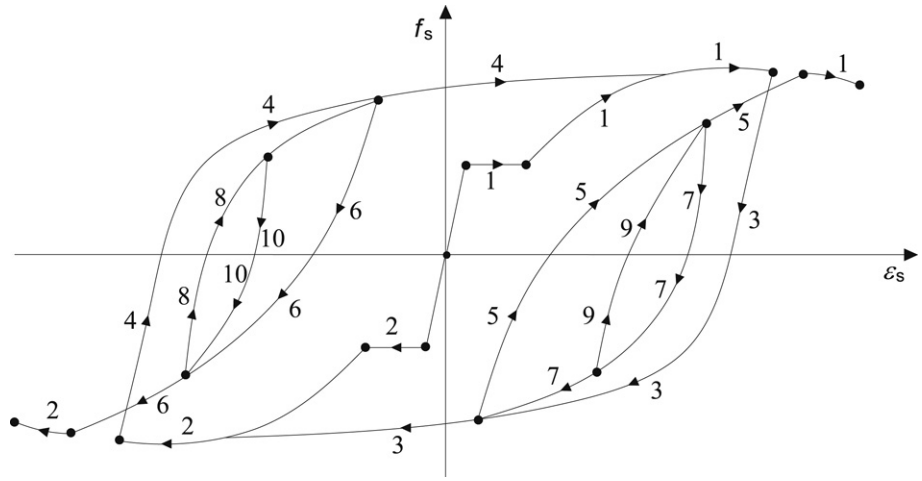

Fig. 19. Schematic representation of the cyclic steel constitutive model.

Table 9
Controlling parameters used in Menegotto Pinto model [24]

Parameter	Rule number							
	3	4	5	6	7	8	9	10
ε_{sai}	ε_{sr}	ε_{sr}	ε_{sr}	ε_{sr}	ε_{sr}	ε_{sr}	ε_{sr}	ε_{sr}
f_{sai}	f_{sr}	f_{sr}	f_{sr}	f_{sr}	f_{sr}	f_{sr}	f_{sr}	f_{sr}
E_{sai}	E_{so}^-	E_{so}^+	E_{so}^+	E_{so}^-	E_{so}^-	E_{so}^+	E_{so}^+	E_{so}^-
ε_{sbi}	$\varepsilon_{s\min}+\varepsilon_{so}^-$	$\varepsilon_{s\max}+\varepsilon_{so}^+$	$\varepsilon_{s\max}+\varepsilon_{so}^+ + \varepsilon_{sa3} - \varepsilon_{sa5} - \frac{f_{sy}^+}{1.2E_s}$	$\varepsilon_{s\min}+\varepsilon_{so}^- + \varepsilon_{sa4} - \varepsilon_{sa6} - \frac{f_{sy}^-}{1.2E_s}$	ε_{sa5}	ε_{sa6}	ε_{sa7}	ε_{sa8}
f_{sbi}	$f_s(\varepsilon_{sb3})$	$f_s(\varepsilon_{sb4})$	$f_s(\varepsilon_{sb5})$	$f_s(\varepsilon_{sb6})$	f_{sa5}	f_{sa6}	f_{sa7}	f_{sa8}
E_{sbi}	$E_s(\varepsilon_{sb3})$	$E_s(\varepsilon_{sb4})$	$E_s(\varepsilon_{sb5})$	$E_s(\varepsilon_{sb6})$	$E_{sa,5}(\varepsilon_{sa5})$	$E_{sa,6}(\varepsilon_{sa6})$	$E_{sa,7}(\varepsilon_{sa7})$	$E_{sa,8}(\varepsilon_{sa8})$

Table 10
Parameters required for Menegotto Pinto model [24]

Parameter	(+)	(−)	Parameter	(+)	(−)
$\varepsilon_{so}^{\pm}$	$\varepsilon_{sa}^+ k_{rev}^- + \varepsilon_{sb}^+(1-k_{rev}^-)$	$\varepsilon_{sa}^-(1-k_{rev}^+) + \varepsilon_{sb}^- k_{rev}^+$	$\varepsilon_{sa}^{\pm}$	$\varepsilon_{so}^+ + \varepsilon_{sh}^+ - \frac{f_y^+}{E_s}$	$\varepsilon_{so}^- + \varepsilon_{sh}^- - \frac{f_y^-}{E_s}$
$\varepsilon_{sb}^{\pm}$	$\varepsilon_{so}^+ + \varepsilon_{s\max} - \frac{f_{s\max}}{E_s}$	$\varepsilon_{so}^- + \varepsilon_{s\min} - \frac{f_{s\min}}{E_s}$	$k_{rev}^{\pm}$	$\exp\left(-\frac{\lvert\varepsilon_{s\min}\rvert}{5000(\varepsilon_{sy}^-)^2}\right)$	$\exp\left(-\frac{\lvert\varepsilon_{s\max}\rvert}{5000(\varepsilon_{sy}^+)^2}\right)$
$E_{so}^{\pm}$	$(1-\Delta\varepsilon_{sa})E_s$	$(1-3\Delta\varepsilon_{sa})E_s$	$R_s^{\pm}$	$20\left(\frac{f_{sy}}{E_s}\right)^{\frac{1}{3}}(1-20\Delta\varepsilon_{sa})$	$16\left(\frac{f_{sy}}{E_s}\right)^{\frac{1}{3}}(1-10\Delta\varepsilon_{sa})$

$\Delta\varepsilon_{sa} = \left|\frac{\varepsilon_{sbi}-\varepsilon_{sai}}{2}\right|$.

than in the intact zones. Therefore, when a steel constitutive model is based on the average stress, this stress is smaller than the one that in reality occurs in the cracked zone. For this reason, steel yield initiation at cracked zones is not correctly simulated if average stress values are adopted to characterize the stress field in a steel bar involved by cracked concrete. To overcome this deficiency an improvement has been implemented in the present constitutive model by means of a technique proposed by Stevens [25], which is based on a reduction of the tensile envelope curve (see Fig. 18), according to the following recommendation

$$\Delta f_s = \frac{75}{\phi_s} f_{ct} C_b, \quad \text{with } f_{ct} \text{ in MPa}$$
$$C_b = \begin{cases} 1 & \text{for steel bars of high adherence} \\ \dfrac{\tau_b}{5 f_{ct}} & \text{in the remaining cases, with } \tau_b = 13.5 \text{ Mpa} \end{cases} \tag{22}$$

where ϕ_s is the bar diameter in millimetres.

The utilization of the cyclic steel model that was described above only requires the following parameters: E_s, f_{sy}, ε_{sh}, f_{sh}, E_{sh}, ε_{su} and f_{su}.

References

[1] FIB. Externally bonded FRP reinforcement for RC structures. Bulletin 14. Lausanne. 2001. p. 138.

[2] ACI. Guide for the design and construction of externally bonded FRP systems for strengthening concrete structures. American concrete institute (Committee 440); 2002. p. 118.

[3] Oehlers DJ, Seracino R, Smith S. Design guideline for RC structures retrofitted with FRP and metal plates: Beams and slabs, SAI global limited standards. 2007. 108 pages [in press] http://www.ecms.adelaide.edu.au/civeng/staff/doehle01.html.

[4] CNR-DT 200. Instructions for design, execution and control of strengthening intervention with FRP. Consiglio Nazionale delle Richerche. 2006. p. 144.

[5] Blaschko M, Zilch K. Rehabilitation of concrete structures with CFRP strips glued into slits. In: Proceedings of 12th int. conf. on composite materials. 1999. p. 7.

[6] Carolin A. Carbon fibre reinforced polymers for strengthening of structural elements. Ph.D. thesis. Division of Structural Engineering. Luleå University of Technology. 2003. p. 190.

[7] El-Hacha R, Rizkalla SH. Near-surface-mounted fiber-reinforced polymer reinforcements for flexural strengthening of concrete structures. ACI Struct J 2004;101(5):717–26.

[8] Barros JAO, Fortes AS. Flexural strengthening of concrete beams with CFRP laminates bonded into slits. J Cem Concr Compos 2005;27(4):471–80.

[9] Barros JAO, Dias SJE. Near surface mounted CFRP laminates for shear strengthening of concrete beams. J Cem Concr Compos 2006;28(3):276–92.

[10] De Lorenzis L, Rizzo A. Behaviour and capacity of RC beams strengthened in shear with NSM FRP reinforcement. In: Proceedings of the 2nd international FIB congress. 2006. Paper ID 10-9.

[11] CEB. RC elements under cyclic loading: State of the art report. Thomas Telford (ed.). Comite Euro-International du Beton; 1996.

[12] Guedes JPSCM. Seismic behaviour of reinforced concrete bridges. Modelling, numerical analysis and experimental assessment. Ph.D. thesis. Joint Research Centre—ISPRA. 1997.

[13] Sena-Cruz JM. Strengthening of concrete structures with near-surface mounted CFRP laminate strips. Ph.D. thesis. Department of Civil Engineering, University of Minho; 2004. http://www.civil.uminho.pt/composites/Publications/2004/PhD2004_001_JSenaCruz.pdf. 2007.
[14] RILEM TC 50-FMC. Determination of fracture energy of mortar and concrete by means of three-point bend tests on notched beams. Mater Struct 1985; 18(106):285–90.
[15] EN 10002-1. Metallic materials. Tensile testing. Part 1: Method of test (at ambient temperature); 1990. p. 35.
[16] EN 196-1. Methods of testing cement. Part 1: Determination of strength. 2005.
[17] ISO 527-5. Plastics—Determination of tensile properties–Part 5: Test conditions for unidirectional fibre-reinforced plastic composites. Geneva (Switzerland): International Organization for Standardization (ISO); 1997. p. 9.
[18] ISO 527-2. Plastics—Determination of tensile properties–Part 2: Test conditions for moulding and extrusion plastics. Geneva (Switzerland): International Organization for Standardization (ISO); 1993. p. 5.
[19] Ferreira DRSM. Pilares de Betão Armado Reforçados com Laminados de Fibras de Carbono (Reinforced concrete columns strengthened with CFRP laminates). M.Sc. thesis. Department of Civil Engineering, University of Minho; 2000. http://www.civil.uminho.pt/composites/Publications/2000/MSc2000_001_DFerreira.pdf. 2007 [in Portuguese].
[20] Sena-Cruz JM, Barros JAO, Azevedo AFM, Ventura Gouveia A. Numerical simulation of the nonlinear behavior of RC beams strengthened with NSM CFRP strips. CMNE/CILAMCE 2007. Paper n° 485 published in CD – FEUP. 2007. 20 pp. http://www.civil.uminho.pt/composites/Publications/2007/CP2007_001_CMNE2007.pdf. 2008.
[21] Chang GA, Mander JB. Seismic energy based fatigue damage analysis of bridge columns: Part I-Evaluation of seismic capacity. Report No. NCEER-94-0006. 1994.
[22] Varma RK, Barros JAO, Sena-Cruz JM. Fibrous model for the simulation of the cyclic behaviour of 3D reinforced concrete frames. Report No. 07-DEC/E-04. Department of Civil Engineering. University of Minho; 2007. p. 90.
[23] Tsai WT. Uniaxial compression stress–strain relation of concrete. J Struct Eng 1988;114(9):2133–6.
[24] Menegotto M, Pinto PE. Method of analysis for cyclically loaded reinforced concrete plane frames including changes in geometry and non-elastic behaviour of elements under combined normal force and bending. In: IABSE symp. on resistance and ultimate deformability of struct. Acted on by well-defined repeated loads. Final report. 1973.
[25] Stevens NJ. Analytical modelling of reinforced concrete subjected to monotonic and reversed loadings. Report No. 87-1. ISBN 0-7727-7088-3. University of Toronto. 1987.
[26] CEB. CEB-FIP model code 1990. Comite Euro-International du Beton. Thomas Telford (ed.). Bulletin d'Information n° 213/214; 1993.